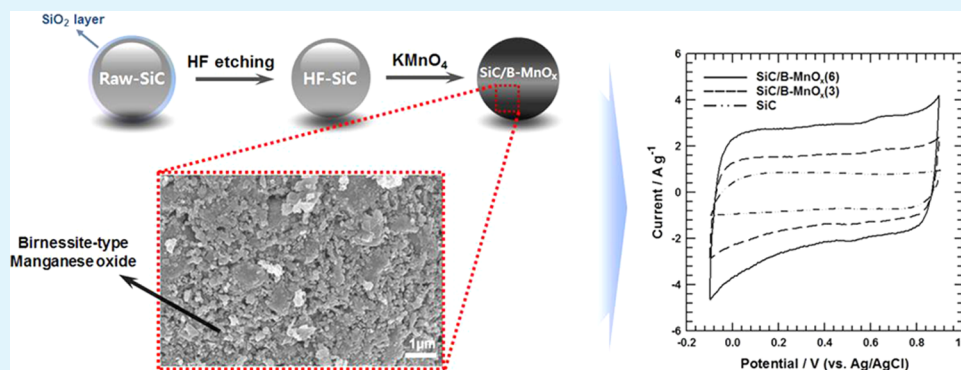# Redox Deposition of Birnessite-Type Manganese Oxide on Silicon Carbide Microspheres for Use as Supercapacitor Electrodes

Myeongjin Kim and Jooheon Kim*

School of Chemical Engineering & Materials Science, Chung-Ang University, Seoul 156-756, Korea

ABSTRACT: Silicon carbide microsphere/birnessite-type MnO_x (SiC/B-MnO_x) composites were prepared by removal of a SiO_2 layer with redox deposition of birnessite-type MnO_x for supercapacitor electrode materials. The characterization studies showed that the birnessite-type MnO_x in the composite was homogeneously deposited on the SiC surface. The capacitive properties of the as-prepared SiC/B-MnO_x electrodes were measured in a three-electrode system using 1 M Na_2SO_4(aq) as the electrolyte. The SiC/B-MnO_x(6) electrode, fabricated using a MnO_x/SiC feeding ratio of 6:1, displayed a specific capacitance of 251.3 F g^{-1} at 10 mV s^{-1}. Such excellent electrochemical performance is attributed to an increase in the electrical conductivity in the presence of silicon carbide, an increase in the effective interfacial area between MnO_x and the electrolyte, and the contact area between MnO_x and silicon carbide. The deposition of birnessite-type MnO_x on a SiC surface may be a prospective fabrication technique for electrode materials for supercapacitors.

KEYWORDS: supercapacitor, silicon carbide, birnessite-type MnO_2, redox deposition, electric double-layer capacitor, pseudocapacitor

1. INTRODUCTION

Over the past few years, because of tremendous energy consumption and the fossil fuel crisis, clean and renewable energy has driven intensive research efforts toward the development of alternative energy storage and delivery systems.[1−4] Environmentally friendly electrochemical capacitors (also called supercapacitors or ultracapacitors), as an effective and practical technology for electrochemical energy storage and conversion, have attracted significant attention, mainly due to their high power density, fast charge/discharge, long life cycle, and bridging function for the power/energy gap between traditional dielectric capacitors having high power output and batteries/fuel cells having high energy storage. These electrochemical capacitors can be employed in a wide range of areas, including hybrid electric vehicles, consumer electronics, memory back-up systems, large industrial equipment, energy management, public transportation, military devices, and so forth.[5−7]

Generally, supercapacitors are classified into either of the following two categories based on their energy-storage mechanism: electric double-layer capacitors (EDLCs) and pseudocapacitors.[8,9] Typical electrode materials for EDLCs consist of high-surface-area carbon, which can store energy by separation of charge in a double layer at the interface between the surface of the electrode and the electrolyte solution, whereas most electrode materials for pseudocapacitors include a conductive polymer and metal oxide, which can achieve energy by redox reactions, electrosorption, or intercalation on the surface of the electrode by specifically adsorbed ions, resulting in a reversible faradaic charge transfer on the electrode. Therefore, to enhance the energy density of supercapacitors, many researchers have used a hybrid material strategy that combines electrode materials for EDLCs with other redox pseudocapacitive materials.[10,11] However, most of the research has been performed by combining graphene with either metal oxides or conductive polymers in supercapacitors.[12−15]

Recently, some new approaches have involved the application of either semiconductor or cermet nanowires for EDLC electrode materials instead of traditional carbon materials such as activated carbon, aerogels, carbon nanotubes, and graphene. Various types of EDLC electrode materials such
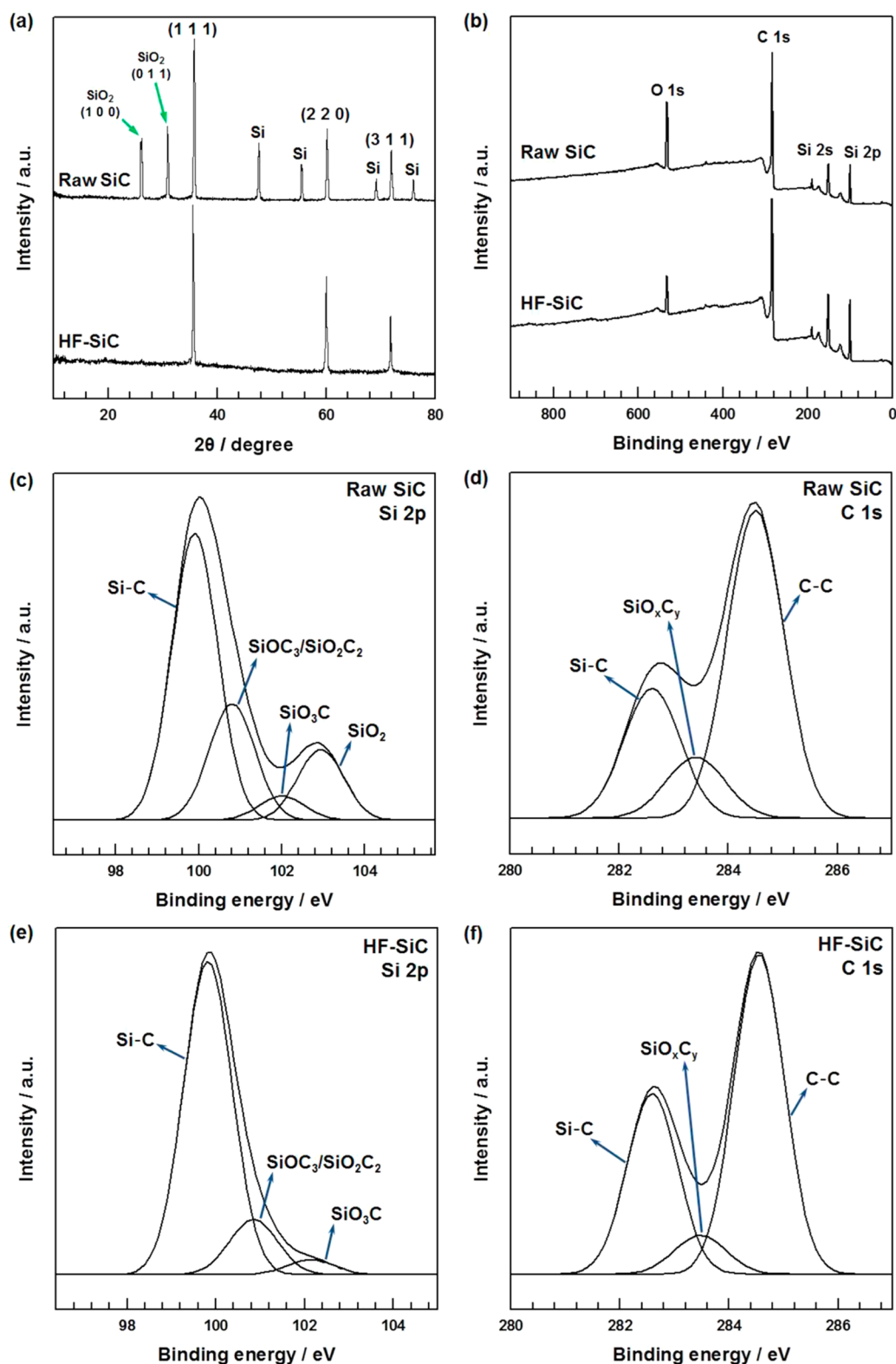
Figure 1. (a) XRD patterns of raw SiC and HF-SiC. (b) XPS wide scan survey spectra of raw SiC and HF-SiC. (c) XPS deconvoluted Si 2p spectrum of raw SiC. (d) XPS deconvoluted C 1s spectrum of raw SiC. (e) XPS deconvoluted Si 2p spectrum of HF-SiC. (f) XPS deconvoluted C 1s spectrum of HF-SiC.

as silicon nanowires, silicon carbide nanowires, titanium nitride nanowires, titanium dioxide nanotubes, and nanowires have attracted much attention recently because of their high specific surface area ($\sim$250 m^2 g^{-1}) and electrical conductivity.[16−21] However, these materials are suitable for microsupercapacitor

electrodes because the working materials are grown directly on the current collector. Therefore, the use of either semiconductor or cermet nanowires as EDLC electrode materials in macroscale supercapacitors has not been reported. Further, the fabrication of hybrid composites in combination with semi-

Table 1. Si 2p Peak Position and the Relative Atomic Percentages of Various Functional Groups in Raw SiC and HF-SiC

	fitting of the Si 2p peak binding energy [eV] (relative atomic percentage [%])			
	Si−C	$SiOC_3/SiO_2C_2$	SiO_3C	SiO_2
raw SiC	99.9 (57.6)	100.8 (23.3)	102 (4.8)	102.9 (14.3)
HF-SiC	99.82 (81.6)	100.85 (14.5)	102.13 (3.9)	

conductors and redox pseudocapacitive materials has not been reported hitherto.

The use of metal oxide electrodes as redox pseudocapacitive materials has attracted considerable interest because of their large capacitance and fast redox kinetics. Among these metal oxide materials, manganese oxide (MnO_2) is considered to be the most promising transition metal oxide for supercapacitors due to its environmental friendliness, high energy density, natural abundance, and low cost.[22,23] Several reports pertaining to the deposition of birnessite-type MnO_2 (B-MnO_2) on graphene have been published. Specifically, Yan et al. suggested the use of hybrid electrode materials prepared by combining graphene with birnessite-type MnO_2, then reducing graphene oxide to graphene by chemical reduction using hydrazine hydrates, followed by the deposition of MnO_2 on the surface of graphene. They showed a specific capacitance of 310 F g^{-1} at a scan rate of 2 mV s^{-1}.[24] Li et al. fabricated graphene/MnO_2 electrode materials via a similar process, wherein the graphene was obtained from thermally reduced graphene oxide. They reported a specific capacitance of 211.5 F g^{-1} at a scan rate of 2 mV s^{-1}.[25] On the basis of these findings, the oxygen-containing functional groups must be removed prior to the deposition of birnessite-type MnO_2 because the deposition reaction occurs by the breaking of the carbon−carbon network.

In this study, silicon carbide microsphere/birnessite-type MnO_x composites were synthesized, with the expectation that the birnessite-type MnO_x would promote reversible pseudocapacitance of the electrodes constructed from the composite and the electrical double-layer properties of silicon carbide microspheres, which act as not only a support for the formation of the birnessite-type MnO_x but also EDLC materials. To obtain a homogeneous deposition of MnO_x, the silicon carbide was treated with hydrofluoric acid (HF) to remove the residual SiO_2 layer adsorbed onto the microspheric SiC particle surface. The morphology and microstructural characteristics of the silicon carbide/birnessite-type MnO_x composites were investigated by X-ray diffraction (XRD), field-emission scanning electron microscopy (FE-SEM), X-ray photoelectron spectroscopy (XPS), and thermogravimetric analysis (TGA). The resulting silicon carbide/birnessite-type MnO_x composites were then applied as an active material in a supercapacitor, and excellent electrochemical properties were observed.

2. EXPERIMENTAL SECTION

2.1. Synthesis of Silicon Carbide/MnO_x Composites. The silicon carbide microspheres were purchased from LG Innotek, Korea. The residual SiO_2 layer adsorbed onto the microspherical SiC particle surface was removed by treatment with HF. In a typical synthesis, 120 g of SiC powder was added to 300 mL of HF solution (the volume ratio between HF and deionized (DI) water was 1:9), and the solution was stirred for 24 h. Then, the mixture was leached with distilled water until the pH of the resultant water became 7−8. These samples are denoted as HF-SiC. The HF-treated microsphere silicon carbide/birnessite-type MnO_x (SiC/B-MnO_x) composites from a MnO_x/SiC feeding ratio of 6:1 (SiC/B-MnO_x(6)) were synthesized as follows: 0.15 g of SiC and 0.5451 g of $KMnO_4$ were added to 100 mL of DI water. Subsequently, the mixture was stirred in a thermostatic bath at

160 °C and refluxed for 12 h. The resulting products were filtered and washed five times with DI water, followed by drying at 60 °C in air for 12 h. The products are denoted as SiC/B-MnO_x(3) and SiC/B-MnO_x(6), corresponding to MnO_x/SiC feeding ratios of 3:1 and 6:1, respectively. For comparison, a pure birnessite-type manganese oxide sample was prepared by dissolving 18 g of $KMnO_4$ in 200 mL of deionized water at 80−90 °C. Then, 500 mL of 1:1 (v/v) HCl was added from a fast-dripping buret (300 mL/min). The black suspension solution was centrifuged and washed five times with distilled water and dried at 100 °C for 6 h in a vacuum oven.

2.2. Characterization Methods. X-ray diffraction (XRD) patterns of the samples were obtained on a New D8-Advance/Bruker-AXS with Cu Kα_1 radiation (0.154 056 nm) at a scanning rate of 1° s^{-1} with a 2θ range of 5°−80°. The morphology of the prepared samples was studied using field-emission scanning electron microscopy (FE-SEM, SIGMA, Carl Zeiss). X-ray photoelectron spectroscopy (XPS) measurements were performed using a VG Microtech ESCA2000 system with a Mg Kα X-ray source (1253.6 eV). Thermogravimetric analysis (TGA) was performed on a TA Instruments TGA-2050 at temperatures of up to 800 °C at a heating rate of 10 °C min^{-1} in air atmosphere.

2.3. Preparation and Characterization of Supercapacitors. The working electrodes were fabricated by first mixing the as-prepared materials and polyvinylidene fluoride (PVDF) using a weight ratio of 95:5; the prepared mixtures were coated on the nickel foam (1 × 1 cm) and dried in a vacuum oven at 60 °C for 6 h. Finally, it was placed between copper plates and pressed under a pressure of 10 MPa for 60 s in room temperature. The loading mass of each electrode was approximately 2.7−3.2 mg cm^{-2}. A three-electrode system consisting of the fabricated working electrode, a platinum counter electrode, and a Ag/AgCl (KCl-saturated) reference electrode was employed in 1 M Na_2SO_4(aq). All measurements, including cyclic voltammetry (CV), galvanostatic charge/discharge characteristics, and EIS measurements, were carried out on a CHI 660C electrochemical workstation. EIS measurements were carried out by applying an AC voltage with 5 mV amplitude in a frequency range from 0.1 to 10^5 Hz at open-circuit potential.

3. RESULTS AND DISCUSSION

The formation of the silicon carbide/birnessite-type MnO_x composites mainly comprised the following two steps: (i) removal of the residual SiO_2 layer adsorbed onto the microspheric SiC particle surface by leaching with HF and (ii) redox deposition of the birnessite-type MnO_x particles onto the SiC surfaces in DI water. The proposed mechanism for depositing MnO_2 onto SiC can be illustrated as follows: $4MnO_4^- + 3C + H_2O \leftrightarrow 4MnO_2 + CO_3^{2-} + 2HCO_3^-$.[24]

First, it is essential to verify the removal of the residual SiO_2 layer formed on the SiC surface by checking for naturally oxidized and oxygen functional groups bonded to the carbon atoms prior to the deposition of the birnessite-type MnO_2. This is because the deposition occurs through the breaking of the carbon−carbon network.[24,25] Figure 1a shows the XRD patterns of the raw SiC and HF-SiC. For the raw SiC, the spectrum contained several peaks that were clearly distinguishable; these peaks were assigned to residual Si, SiO_2, and β polytype SiC (β-SiC). Three characteristics peaks at 2θ = 35.6°, 60°, and 71.7°, which were assigned to the (1 1 1), (2 2 0), and (3 1 1) reflections, respectively, were correlated to the face-

9038

dx.doi.org/10.1021/am406032y | ACS Appl. Mater. Interfaces 2014, 6, 9036−9045

centered cubic (fcc) β-SiC structure in accordance with the reference data (JCPDS 29-1129, a = 4.3589 Å).[26,27] The XRD pattern of HF-SiC showed that only β-SiC remained after the HF treatment, showing that the residual Si and SiO_2 were effectively removed. Figure 1b shows the XPS survey spectra of the raw SiC and HF-SiC. The raw SiC consisted of only three elements, namely C, Si, and O. However, the O 1s signal decreased dramatically in the spectra of HF-SiC, implying that the oxygen atoms that existed as SiO_2 on the raw SiC surface were effectively removed through the HF treatment. To obtain the detailed surface information on the raw SiC and HF-SiC, the Si 2p and C 1s core-level spectra of each sample were deconvoluted; the results are shown in Figure 1c−f and summarized in Tables 1 and 2. Moreover, the relative atomic

Table 2. C 1s Peak Position and the Relative Atomic Percentages of Various Functional Groups in Raw SiC and HF-SiC

	fitting of the C 1s peak binding energy [eV] (relative atomic percentage [%])		
	Si−C	SiO_xC_y	C−C
raw SiC	282.6 (25.9)	283.4 (12.8)	284.5 (61.3)
HF-SiC	282.59 (33.4)	283.47 (7.5)	284.55 (59.1)

percentage is obtained by taking the ratio of the each peak areas in the Si 2p and C 1s core-level spectra. The Si 2p region of the spectrum measured from the surface of the raw SiC (Figure 1c) showed that besides the strong Si−C peak at the binding energy of 99.9 eV, some intermediate oxidation products of SiC also existed on the surface. These were interpreted as $SiOC_3$ + SiO_2C_2 at 100.8 eV, SiO_3C at 102 eV, and SiO_2 at 102.9 eV.[28] The C 1s core level (Figure 1d) showed strong binding energy peaks of Si−C bonds at 282.6 eV and C−C bonds at 284.5 eV, with several binding energy peaks of SiO_xC_y at 283.4 eV. In contrast to the spectra of the raw SiC, the Si 2p spectrum of HF-SiC (Figure 1e) showed that the area of the Si−C peak was predominant, whereas the areas of $SiOC_3$ + SiO_2C_2, and SiO_3C decreased dramatically. Moreover, the SiO_2 peak disappeared, indicating that the residual SiO_2 layer on the raw SiC surface was effectively removed. Moreover, as shown in the deconvoluted C 1s spectrum (Figure 1f), the peak area of SiO_xC_y decreased dramatically after the HF treatment.

Figure 2 shows the XRD patterns of HF-SiC, SiC/B-MnO$_x$(3), SiC/B-MnO$_x$(6), and B-MnO$_x$. The diffraction peaks of the as-synthesized SiC/B-MnO$_x$ confirmed the monoclinic lamellar structure of the birnessite-type MnO_2 (JCPDS 42-1317), with three broad peaks at 2θ around 12°, 37°, and 66° assigned to (0 0 1), (1 1 0) and (0 2 0) reflections.[24,29] Interestingly, the diffraction peaks of HF-SiC nearly disappeared, showing that homogeneous composites were formed, wherein the HF-SiC surface was covered by nanoscale birnessite-type MnO$_x$. This outcome correlated well with the results of previous studies, wherein the diffraction peaks either weakened or disappeared.[30] Moreover, the comparison of SiC/B-MnO$_x$(3) and SiC/B-MnO$_x$(6) showed that an increase in the MnO$_x$ content of the composites led to a gradual increase in the intensities of the diffraction peaks.[31]

The detailed surface information on HF-SiC, SiC/B-MnO$_x$(3), and SiC/B-MnO$_x$(6) was collected using XPS, and the results are shown in Figure 3. As shown in Figure 3a, the XPS survey spectrum of HF-SiC consisted of carbon, oxygen, and silicon. However, a Mn signal (2p$_{3/2}$, 2p$_{1/2}$) was observed
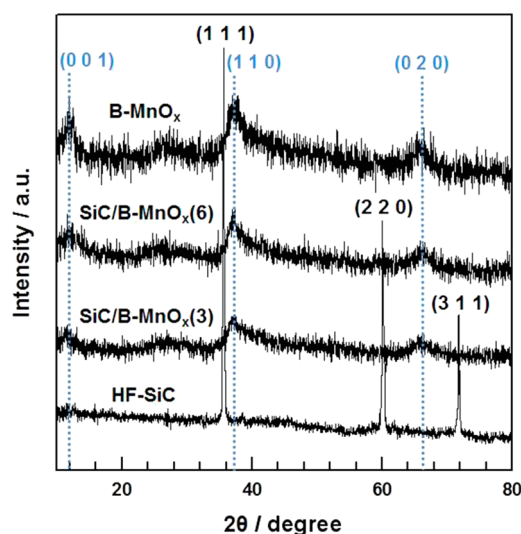

Figure 2. XRD patterns of HF-SiC, SiC/B-MnO$_x$(3), SiC/B-MnO$_x$(6), and B-MnO$_x$.

in the spectra of SiC/B-MnO$_x$(3) and SiC/B-MnO$_x$(6), showing that the birnessite-type MnO$_x$ was successfully deposited on the surface of the SiC particles. Interestingly, the C and Si peaks decreased dramatically because the birnessite-type MnO$_x$ fully covered the SiC surface, which is in accordance with the XRD analysis. With an increase in the MnO$_x$ content in the composites, the peaks of Mn 2p$_{3/2}$ and Mn 2p$_{1/2}$ increased gradually in intensity, as supported by the XRD analysis.[32] When manganese oxide is used as the supercapacitor electrode material, it is important to consider the valence of manganese. Therefore, the manganese oxidation state in the prepared SiC/B-MnO$_x$ was investigated using the Mn 2p, Mn 3s, and O 1s core-level spectra; the results are shown in Figure 3b−d, respectively. Figure 3b shows the deconvoluted Mn 2p core-level spectra of SiC/B-MnO$_x$(6), wherein the Mn 2p$_{3/2}$ and Mn 2p$_{1/2}$ peaks are located at 642.1 and 653.8 eV, respectively. The spin-energy separation between the Mn 2p$_{3/2}$ and Mn 2p$_{1/2}$ peaks was observed by 11.7 eV, which is in agreement with the results previously reported for birnessite-type MnO$_2$, suggesting the presence of a large number of tetravalent Mn.[24] However, it was challenging to determine the precise oxidation state of manganese solely from the Mn 2p core level owing to either the broadening or tailing of peaks at lower binding energies.[33] Therefore, the oxidation state of manganese can be determined accurately by analysis of the Mn 3s and O 1s core-level spectra.[34] As shown in Figure 3c, the Mn 3s core-level peak of SiC/B-MnO$_x$(6) showed peak splitting, and peak energy separation (ΔE) was observed at 4.84 eV. The reason for the peak splitting and doublet in the Mn 3s core-level spectra is that the electrons of the 3s and 3d orbitals caused parallel spin coupling during the photoelectron ejection.[35] According to an approximately linear relationship between ΔE and the oxidation state of manganese reported by Toupin et al., the average oxidation state of Mn was 3.8 for the as-synthesized birnessite-type MnO$_x$ in the SiC/B-MnO$_x$(6) composite.[33] Moreover, the O 1s core-level spectrum was also investigated in order to analyze the change of manganese oxidation state during redox-switching.[36] As shown in Figure 3d, there are three kinds of oxygen bonds in the O 1s spectrum, such as water (H−O−H) and low concentrations of SiO_xC_y at 532.4 eV, hydroxide (Mn−O−H) at 531.2 eV, and Mn−O−
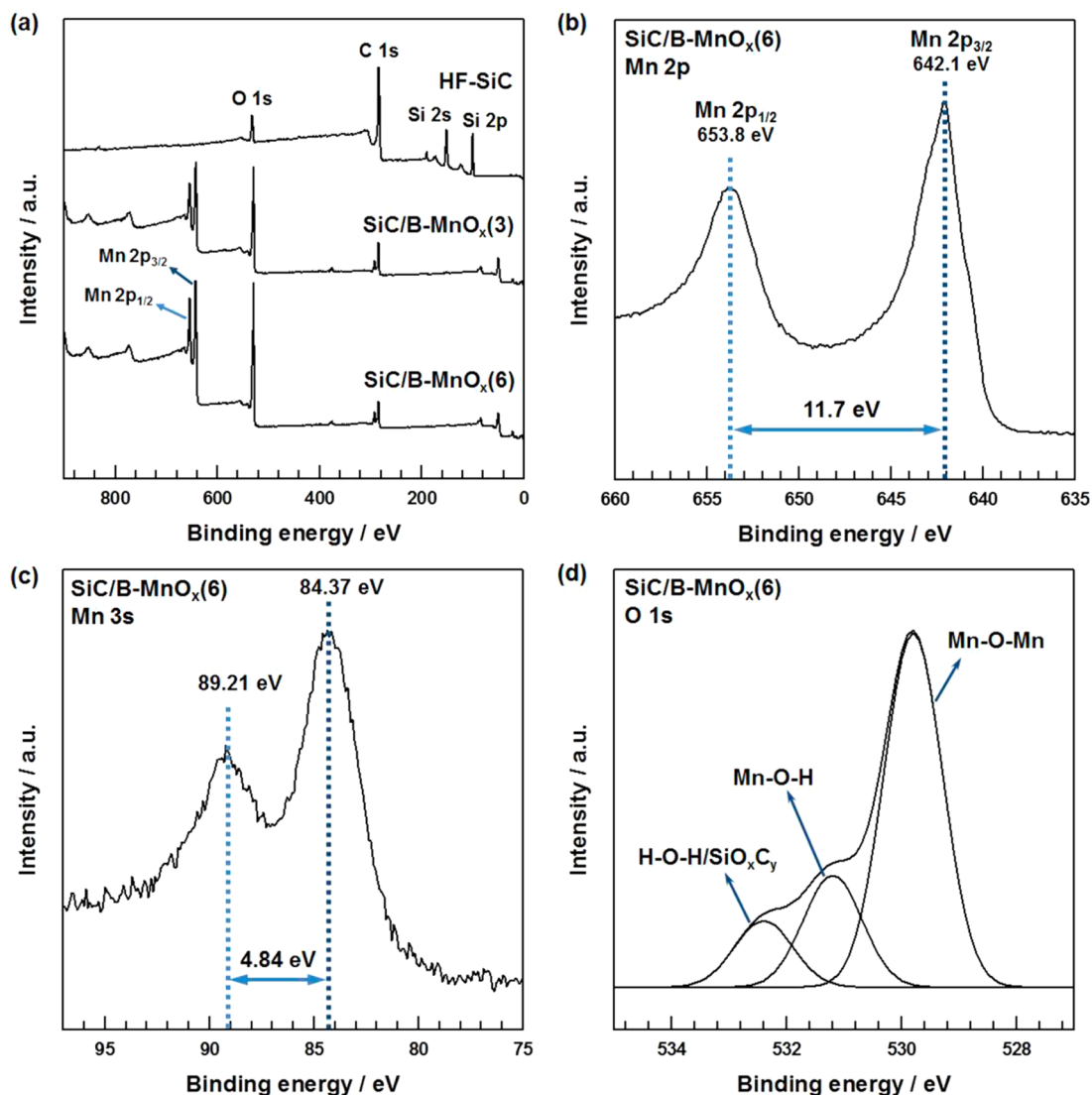
9039

dx.doi.org/10.1021/am406032y | ACS Appl. Mater. Interfaces 2014, 6, 9036−9045

Figure 3. (a) XPS wide scan survey spectra of HF-SiC, SiC/B-MnO$_x$(3) and SiC/B-MnO$_x$(6). (b) XPS spectra of Mn 2p peaks of the SiC/B-MnO$_x$(6) composite. (c) XPS spectra of Mn 3s peaks of the SiC/B-MnO$_x$(6) composite. (d) XPS deconvoluted O 1s spectra of the SiC/B-MnO$_x$(6) composite.

Mn bonds at 529.8 eV, which consists of MnOOH and MnO$_2$.[34] Consequently, the average oxidation state of manganese can be obtained by calculating the area of the peaks associated with Mn−O−Mn and Mn−O−H using the following formula:[36]

manganese oxidation state

$$= [IV \cdot (S_{Mn-O-Mn} - S_{Mn-O-H}) + III \cdot S_{Mn-O-H}]/S_{Mn-O-Mn} \quad (1)$$

where S stands for the signal of the different components of the O 1s spectrum. As shown in Figure 3d, the relative peak areas of Mn−O−Mn, Mn−O−H, and H−O−H/SiO$_x$C$_y$ are 66.5, 21.1, and 12.4%, respectively. Therefore, the average oxidation state of manganese in the as-synthesized birnessite-type MnO$_x$ in the SiC/B-MnO$_x$(6) composite was 3.7, which is similar to the value obtained from the Mn 3s core-level spectrum. As a result, the as-prepared birnessite-type MnO$_x$ in the SiC/B-MnO$_x$ composite is composed of both trivalent and tetravalent systems, indicating that a mixed valence system would be a great advantage during the charge/discharge process because

the coexistence of trivalent and tetravalent Mn would facilitate the formation of more ionic defects.[37]

The compositions of the as-prepared SiC/B-MnO$_x$(3) and SiC/B-MnO$_x$(6) composites were further investigated using TGA (Figure 4). The experiments were conducted at temperatures of up to 800 °C at a heating rate of 10 °C min^{-1} in air atmosphere. Under these conditions, HF-SiC exhibited only 0.4% weight loss, whereas the MnO$_2$ was converted into Mn$_2$O$_3$.[38] Figure 4 shows the representative TGA curves of HF-SiC, SiC/B-MnO$_x$(3), SiC/B-MnO$_x$(6), and birnessite-type MnO$_x$ (B-MnO$_x$). The weight losses of HF-SiC, SiC/B-MnO$_x$(3), SiC/B-MnO$_x$(6), and B-MnO$_x$ were found to be 0.4, 6.4, 8.9, and 14.3%, respectively. Accordingly, the mass ratios of B-MnO$_x$/(HF-SiC) for SiC/B-MnO$_x$(3) and SiC/B-MnO$_x$(6) were derived as 0.76:1 and 1.57:1, respectively. Therefore, with an increase in the MnO$_x$ content in the SiC/B-MnO$_x$ composites, the mass ratios of B-MnO$_x$/(HF-SiC) also increased; this behavior was in good agreement with the results of the XRD and XPS measurements.

The morphology and structure of the as-prepared composites were further studied using FE-SEM analysis. Figure 5 shows the
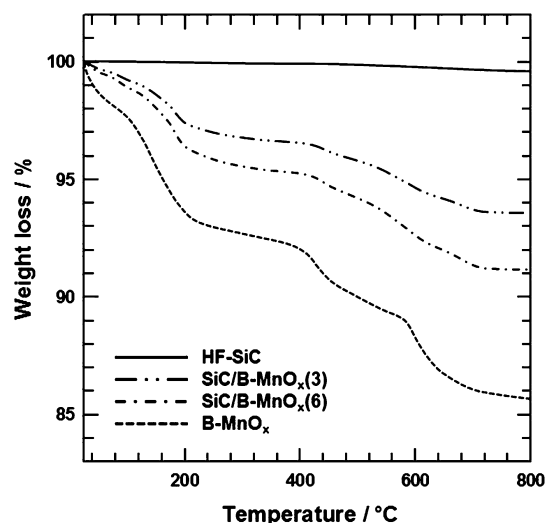
Figure 4. TGA curves of HF-SiC, SiC/B-MnO$_x$(3), SiC/B-MnO$_x$(6) and B-MnO$_x$.

FE-SEM images of the SiC, birnessite-type MnO$_x$, and SiC/B-MnO$_x$(6) composites. The SiC particles (Figure 5a) are spherical, with an average particle diameter of ~30 μm and a rough surface morphology. Figure 5b shows the morphologies of the as-obtained birnessite-type MnO$_x$, which exhibits a flower-like structure.[39] Figure 5c,d represents the low and high magnifications of the FE-SEM images of SiC/B-MnO$_x$(6) composite, respectively. The birnessite-type MnO$_x$ was uniformly formed on the SiC surface. The removal of the residual SiO$_2$ layer on the SiC surface can facilitate the homogeneous deposition of nanostructures formed on the SiC

surface by breaking of the carbon–carbon network.[24,25,39] Such homogeneously deposited birnessite-type MnO$_x$ on the SiC surface is attributable to the increase of specific surface area, which was accessible to the electrolyte ions to the exterior and interior pore surfaces, as well as to the shorter transport/diffusion path lengths for both ions and electrons.[40]

Cyclic voltammetry (CV), galvanostatic charge/discharge, and EIS measurements were generally applied to evaluate the electrochemical properties of the as-prepared electrode samples. Figure 6a shows the CV curves of the SiC, SiC/B-MnO$_x$(3), and SiC/B-MnO$_x$(6) electrodes at a scan rate of 10 mV s^{-1} in a 1 M Na$_2$SO$_4$ electrolyte. The CV curve of the SiC electrode had an ideal rectangular shape without obvious redox peaks, showing that the SiC exhibited ideal capacitive behavior.[41] The spherical morphology of SiC enhanced the surface area and formed pores for ion-buffering reservoirs, enhancing the electric double-layer capacity. Moreover, the β polytype of SiC exhibited an outstanding electronic conductivity (~8.2 S cm^{-1}) because β-SiC possessed the smallest band gap (~2.4 eV) and one of the largest electron mobilities (~800 cm^2 V^{-1} s^{-1} in a low-doped material) of all the known SiC polytypes.[42] Therefore, such beneficial capacitive characteristics of the SiC electrode are attributed to the synergistic effect of the excellent electrical conductivity, electric double-layer capacity, and highly electroactive areas. Clearly, the integrated area of the CV curves for all the SiC/B-MnO$_x$ composite electrodes was much larger than that of the SiC electrode, indicating superior electrochemical performance. These excellent electrochemical properties can be explained by the following three reasons: (i) the microspherical silicon carbide in the composites acted not only as electrical conductive channels but also as support for the deposition of birnessite-type MnO$_x$.
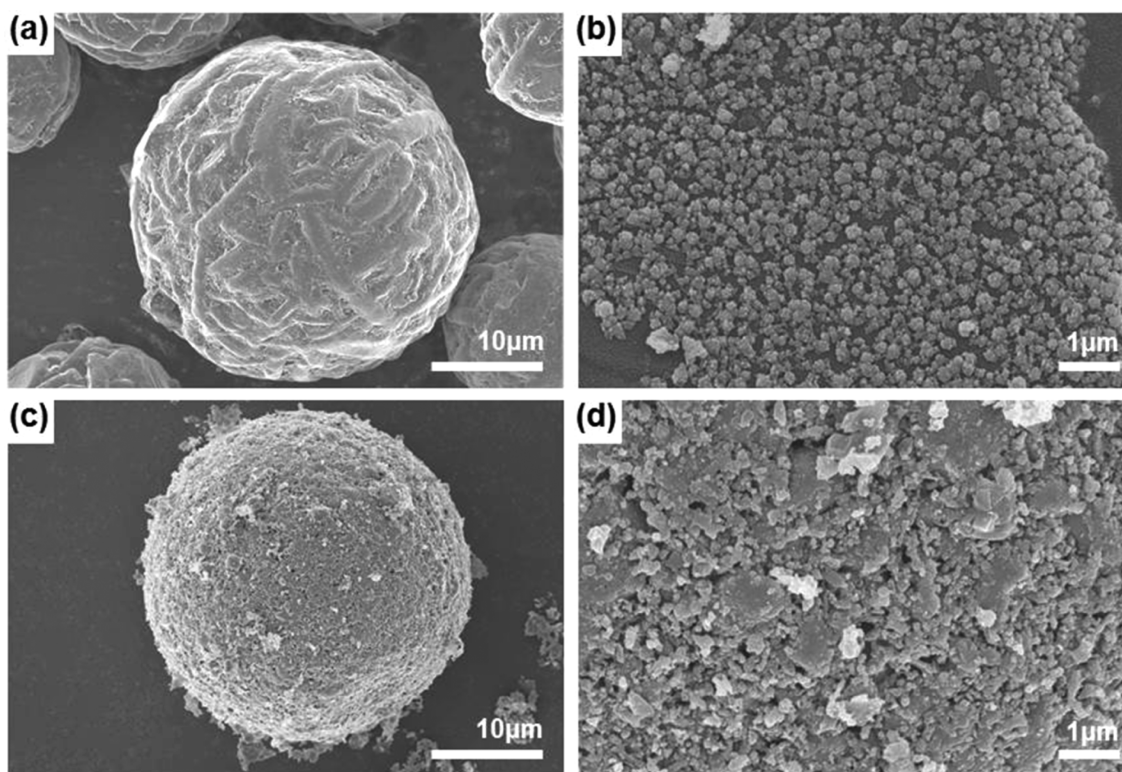

Figure 5. (a) FE-SEM image of SiC particles. (b) FE-SEM image of birnessite-type MnO$_x$. (c) Low-magnification FE-SEM image of SiC/B-MnO$_x$(6). (d) High-magnification FE-SEM image of SiC/B-MnO$_x$(6).
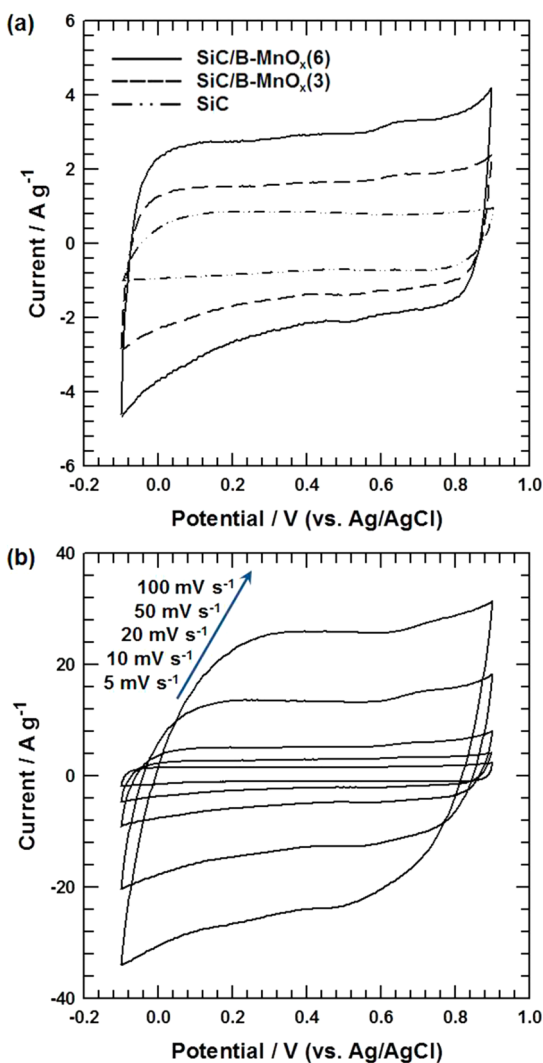
Figure 6. (a) CV curves of SiC, SiC/B-MnO$_x$(3) and SiC/B-MnO$_x$(6) electrodes at a scan rate of 10 mV s^{-1}. (b) CV curves of SiC/B-MnO$_x$(6) electrode measured as different scan rates of 5, 10, 20, 50, and 100 mV s^{-1}.

Moreover, the excellent interfacial contact between the birnessite-type MnO$_x$ and SiC facilitated the fast transportation of electrons throughout the electrode matrix. (ii) The birnessite-type MnO$_x$ is beneficial to the specific surface area of the SiC/B-MnO$_x$ composite electrodes in that it can facilitate the formation of pores for ion-buffering reservoirs, resulting in improvement of the diffusion rate of Na$^+$ ions during the charge/discharge process.[43] (iii) The birnessite-type MnO$_x$ attached to the SiC surface can easily participate the pseudocapacitive redox reactions, resulting in maximizing the pseudocapacitive contribution. The mechanism of charge storage of MnO$_2$ in a neutral Na$_2$SO$_4$(aq) may proceed via two reactions.[44] The first concerns the redox reaction, in which Na$^+$ ions are inserted into and extracted out of the electrode. This redox reaction can be expressed as

$$MnO_2 + Na^+ + e^- \leftrightarrow MnOONa \qquad (2)$$
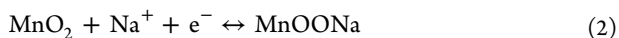
The second reaction concerns the adsorption and desorption of Na$^+$ ions at the MnO$_2$ surface, which can be expressed as

$$(MnO_2)_{surface} + Na^+ + e^- \leftrightarrow (MnO_2^- Na^+)_{surface} \qquad (3)$$
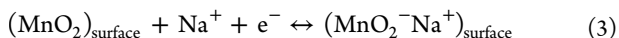
The proposed mechanism involves a redox reaction between the trivalent and tetravalent oxidation states of manganese. As confirmed by XPS analysis, the birnessite-type MnO$_x$ in SiC/B-MnO$_x$ composites is composed of both trivalent and tetravalent systems, which improves the capacitance of manganese oxide. As a result, these redox reactions would cause pseudocapacitance, which can enhance the supercapacitance. In a comparison of the SiC/B-MnO$_x$(3) and SiC/B-MnO$_x$(6) electrodes, the integrated area of the CV curve for SiC/B-MnO$_x$(6) electrode was much larger than that of the SiC/B-MnO$_x$(3) electrode, owing to the deposition of a much larger amount of the birnessite-type MnO$_x$, which was confirmed by TGA analysis. To further investigate the advantages of SiC/B-MnO$_x$ composites as supercapacitor electrodes, the rate-dependent CV of the SiC/B-MnO$_x$(6) electrode over a wide range of scan rates is shown in Figure 6b. It is seen that the rectangular area apparently increases and there is no obvious distortion in the CV loops with the incremental increase of the scan rate, implying a desirable rate capability and good capacitive behavior.

The specific capacitances (C_s) were calculated from the CV curves using the following equation:[45]

$$C_s = \frac{1}{v(V_c - V_a)} \int_{V_a}^{V_c} I(V) dV \qquad (4)$$

where C_s is the specific capacitance (F g^{-1}), v is the potential scan rate (mV s^{-1}), $V_c - V_a$ represents the sweep potential range (V), and I(V) denotes the response current density (A g^{-1}). Figure 7 shows the relationships between C_s and the scan
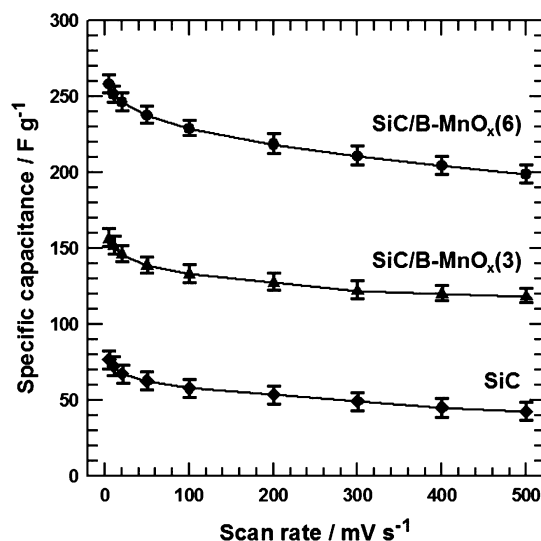

Figure 7. Specific capacitance of SiC, SiC/B-MnO$_x$(3) and SiC/B-MnO$_x$(6) electrodes at different scan rates.

rates of the SiC, SiC/B-MnO$_x$(3), and SiC/B-MnO$_x$(6) electrodes. The calculated C_s values of the SiC, SiC/B-MnO$_x$(3), and SiC/B-MnO$_x$(6) electrodes at 10 mV s^{-1} were 72.4, 151.6, and 251.3 F g^{-1}, respectively. The SiC/B-MnO$_x$(6) electrode showed the highest specific capacitance over the entire range of scan rates. This result could be attributed to both the intrinsic EDL capacitance of SiC and the pseudocapacitive reaction owing to the homogeneous dispersion of the nanosized birnessite-type MnO$_x$. Moreover, at a low scan rate (2 mV s^{-1}), the diffusion of ions from the electrolyte can access almost all the available pores of the

electrode, leading to a complete insertion reaction and therefore a higher specific capacitance. With the incremental increase of scan rate, the effective interaction between the ions and the electrode is greatly reduced, and as a result, there is a reduction in capacitance.[46,47] The pseudocapacitance due to the birnessite-type MnO_x in the composite was calculated by subtracting the EDLC capacitance contribution from the SiC substrate using the following equation:[38]

$$C_{MnO_2} = (C_{SiC/MnO_2} - C_{SiC} \times SiC\%)/MnO_2\% \qquad (5)$$

where C_{MnO_2}, C_{SiC/MnO_2}, and C_{SiC} are the specific capacitance of the birnessite-type MnO_x, SiC/B-MnO_x (SiC/B-MnO_x(3) and SiC/B-MnO_x(6) in this calculation), and SiC, respectively, and SiC% and MnO_2% are the weight percentages of the SiC and birnessite-type MnO_x in the composites, respectively. Because the specific capacitance of the SiC electrode was found to be 72.4 F g^{-1} at a scan rate of 10 mV s^{-1}, the specific capacitances of the birnessite-type MnO_x were calculated to be 255.7 and 364.7 F g^{-1} for SiC/B-MnO_x(3) and SiC/B-MnO_x(6), respectively.

Figure 8 represents the galvanostatic charge/discharge curves for SiC, SiC/B-MnO_x(3), and SiC/B-MnO_x(6) electrodes

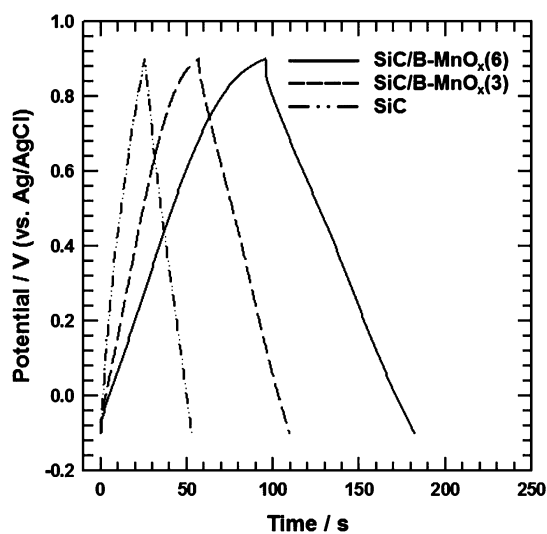**Figure 9.** Nyquist plots of SiC, SiC/B-MnO_x(3), and SiC/B-MnO_x(6) electrodes.

Figure 8. Galvanostatic charge/discharge curves of SiC, SiC/B-MnO_x(3) and SiC/B-MnO_x(6) electrodes at a current density of 10 mA cm^{-2}.

measured between −0.1 and +0.9 V at a current density of 10 mA cm^{-2}. The shapes of the curves for the SiC/B-MnO_x(3) and SiC/B-MnO_x(6) electrodes exhibit a typical triangular symmetrical distribution with a slight curvature, indicating the combination of electric double-layer and pseudocapacitive contributions.[43] Moreover, upon comparing the discharge curves, the SiC/B-MnO_x(6) electrode showed the longest discharging time as compared to the SiC and SiC/B-MnO_x(3) electrodes, implying that the SiC/B-MnO_x(6) electrode exhibited the largest specific capacitance value, which is the same as the results from the pattern of the CV curve and specific capacitance behavior.

EIS was performed to further evaluate the electrochemical performance. Nyquist plots of the SiC, SiC/B-MnO_x(3), and SiC/B-MnO_x(6) electrodes are displayed in Figure 9. All the impedance plots are composed of a semicircle in the high-frequency range and a straight line in the low-frequency range.
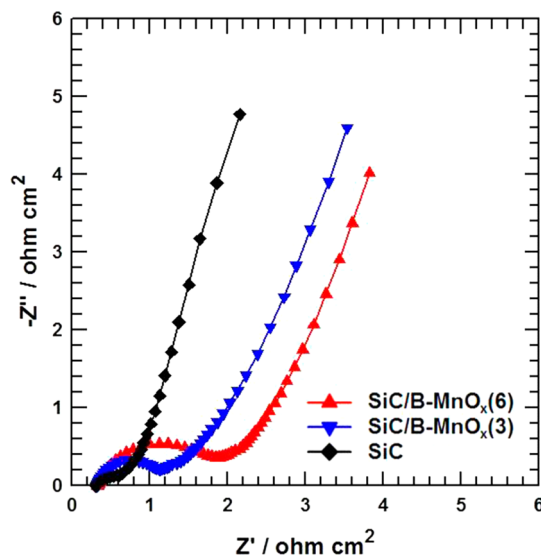
In the high-frequency region, the real axis intercept represents the internal resistance, which includes the sum of the contact resistance of the interface between the active material and the current collector, the intrinsic resistance of the active material, and the ionic resistance of the electrolyte; the semicircle corresponds to the charge transfer resistance (R_{ct}).[48] In the Nyquist plots, all electrodes exhibit a small real axis intercept, suggesting a low interfacial resistance between the current collector and the active material, active material resistance, and electrolyte resistance. Moreover, in a comparison of the Nyquist plots of the SiC, SiC/B-MnO_x(3), and SiC/B-MnO_x(6) electrodes, a major difference was the R_{ct} value, which is related to both the electrical conductivity of the electrodes and faradaic reactions. It is clear that the SiC/B-MnO_x(6) electrode exhibited the highest R_{ct} value among the SiC/B-MnO_x composite electrodes, corresponding to an increasing R_{ct} value with increasing MnO_x content, which was confirmed by the TGA analysis, as illustrated in Figure 4.[25] The straight line in the low-frequency range of all electrodes is related to the diffusive resistance of the electrolyte into the interior of the electrode and ion diffusion into the electrode.[25] The almost vertical shape, representing facile electrolyte ion diffusion to the active material, suggests the ideal capacitive behavior of the electrodes.[49]

Cycle stability behavior is crucial for supercapacitors. The cycling stability of the SiC/B-MnO_x(6) electrode was evaluated using CV at a scan rate of 10 mV s^{-1} for 1000 cycles. As shown in Figure 10, the specific capacitance of SiC/B-MnO_x(6) decreased gradually over the initial 500 cycles. The capacitance retention for the SiC/B-MnO_x(6) electrode was 94.43% after 1000 cycles, showing the excellent cycle stability of the SiC/B-MnO_x(6) electrode. The capacitance of the SiC/B-MnO_x(6) electrode after 1000 cycles was also smaller than that after the first cycle, which may be attributed to the loss of the active materials caused by dissolution and detachment during the charge/discharge process.[50]

4. CONCLUSIONS

SiC/B-MnO_x composites were synthesized and their structural characteristics and electrochemical properties were evaluated in
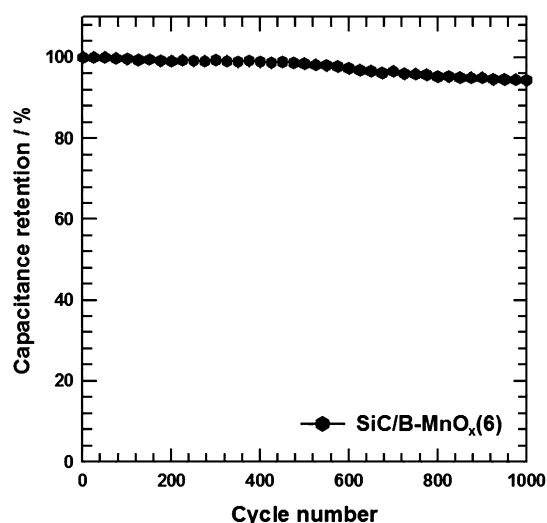
Figure 10. Cycling stability of SiC/B-MnO$_x$(6) electrode measured at a scan rate of 10 mV s^{-1}.

order to investigate their potential application in supercapacitors. The SiC electrode showed a specific capacitance of 72.4 F g^{-1} at a scan rate of 10 mV s^{-1}, which was attributed to the synergistic effect of the excellent electrical conductivity, electric double-layer capacity, and highly electroactive areas. The SiC/B-MnO$_x$ composite was synthesized by redox deposition of birnessite-type MnO$_x$ on the HF-SiC surface. The specific capacitance of the SiC/B-MnO$_x$(6) composite electrode was 251.3 F g^{-1} at a scan rate of 10 mV s^{-1}. After 1000 cycles, the capacitance retention for the SiC/B-MnO$_x$(6) electrode was 94.43%, showing excellent cycle stability. Therefore, our new approach, which is the combination of microspherical silicon carbide as EDLC materials and birnessite-type MnO$_2$ as pseudocapacitive materials, yielded encouraging results, suggesting potential application in supercapacitors and in other power source systems.

■ AUTHOR INFORMATION

Corresponding Author

*J. Kim. Tel: +82-2-820-5763. Fax: +82-2-812-3495. E-mail: jooheonkim@cau.ac.kr.

Notes

The authors declare no competing financial interest.

■ ACKNOWLEDGMENTS

■ REFERENCES

(1) Subramanian, V.; Zhu, H.; Vajtai, R.; Ajayan, P. M.; Wei, B. Hydrothermal Synthesis and Pseudocapacitance Properties of MnO$_2$ Nanostructures. *J. Phys. Chem. B* **2005**, *109*, 20207−20214.

(2) Mohana, A. L.; Estaline, R. F.; Imran, A.; Ramaprabhu, J. S. Asymmetric Flexible Supercapacitor Stack. *Nanoscale Res. Lett.* **2008**, *3*, 145−151.

(3) Karina, A. C.-G.; Monica, L.-C.; Nieves, C.-P.; Pedro, G.-R. Nanocomposites Hybrid Molecular Materials for Application in Solid-State Electrochemical Supercapacitors. *Adv. Funct. Mater.* **2005**, *15*, 1125−1133.

(4) Chow, J.; Kopp, R. J.; Portney, P. R. Energy Resources and Global Development. *Science* **2003**, *302*, 1528−1531.

(5) Wen, Z.; Wang, X.; Mao, S.; Bo, Z.; Kim, H.; Cui, S.; Lu, G.; Feng, X.; Chen, J. Crumpled Nitrogen-Doped Grapheme Nanosheets with Ultrahigh Pore Volume for High-Performance Supercapacitor. *Adv. Mater.* **2012**, *24*, 5610−5616.

(6) Kotz, R.; Carlen, M. Principles and Applications of Electrochemical Capacitors. *Electrochim. Acta* **2000**, *45*, 2483−2498.

(7) Chen, Z.; Qin, Y.; Weng, D.; Xiao, Q.; Peng, Y.; Wang, X.; Li, H.; Wei, F.; Lu, Y. Design and Synthesis of Hierarchical Nanowire Composites for Electrochemical Energy Storage. *Adv. Funct. Mater.* **2009**, *19*, 3420−3426.

(8) Bose, S.; Kuila, T.; Mishra, A. K.; Rajasekar, R.; Kim, N. H.; Lee, J. H. Carbon-based Nanostructured Materials and Their Composites As Supercapacitor Electrodes. *J. Mater. Chem.* **2012**, *22*, 767−784.

(9) Jiang, H.; Ma, J.; Li, C. Z. Mesoporous Carbon Incorporated Metal Oxide Nanomaterials As Supercapacitor Electrodes. *Adv. Mater.* **2012**, *24*, 4197−4202.

(10) Simon, P.; Gogotsi, Y. Materials for Electrochemical Capacitors. *Nat. Mater.* **2008**, *7*, 845−854.

(11) Chou, S. L.; Wang, J. Z.; Chew, S. Y.; Liu, H. K.; Dou, S. X. Electrodeposition of MnO$_2$ Nanowires on Carbon Nanotube Paper As Free-Standing, Flexible Electrode for Supercapacitors. *Electrochem. Commun.* **2008**, *10*, 1724−1727.

(12) Dong, X. C.; Xu, H.; Wang, X. W.; Huang, Y. X.; Park, M. B. C.; Zhang, H.; Wang, L. H.; Huang, W.; Chen, P. 3D Graphene-Cobalt Oxide Electrode for High-Performance Supercapacitor and Enzymeless Glucose Detection. *ACS Nano* **2012**, *6*, 3206−3213.

(13) Chen, S.; Zhu, J.; Wang, X. One-Step Synthesis of Graphene-Cobalt Hydroxide Nanocomposites and Their Electrochemical Properties. *J. Phys. Chem. C* **2010**, *114*, 11829−11834.

(14) Xia, X.; Hao, Q.; Lei, W.; Wang, W.; Sun, D.; Wang, X. Nanostructured Ternary Composites of Graphene/Fe$_2$O$_3$/Polyaniline for High-Performance Supercapacitors. *J. Mater. Chem.* **2012**, *22*, 16844−16850.

(15) Xiang, C.; Li, M.; Zhi, M.; Manivannan, A.; Wu, N. A Reduced Graphene Oxide/Co$_3$O$_4$ Composite for Supercapacitor Electrode. *J. Power Sources* **2013**, *226*, 65−70.

(16) Choi, J. W.; McDonough, J.; Jeong, S.; Yoo, J. S.; Chan, C. K.; Cui, Y. Stepwise Nanopore Evolution in One-Dimensional Nanostructures. *Nano Lett.* **2010**, *10*, 1409−1413.

(17) Alper, J. P.; Vincent, M.; Carraro, C.; Maboudian, R. Silicon Carbide Coated Silicon Nanowires As Robust Electrode Material for Aqueous Micro-Supercapacitor. *Appl. Phys. Lett.* **2012**, *100*, 163901−163904.

(18) Alper, J. P.; Kim, M. S.; Vincent, M.; Hsia, B.; Radmilovic, V.; Carraro, C.; Maboudian, R. Silicon Carbide Nanowires As Highly Robust Electrodes for Micro-Supercapacitors. *J. Power Sources* **2013**, *230*, 298−302.

(19) Lu, X.; Wang, G.; Zhai, T.; Yu, M.; Xie, S.; Ling, Y.; Liang, C.; Tong, Y.; Li, Y. Stabilized TiN Nanowire Arrays for High-Performance and Flexible Supercapacitors. *Nano Lett.* **2012**, *12*, 5376−5381.

(20) Lu, X.; Wang, G.; Zhai, T.; Yu, M.; Gan, J.; Tong, Y.; Li, Y. Hydrogenated TiO$_2$ Nanotube Arrays for Supercapacitors. *Nano Lett.* **2012**, *12*, 1690−1696.

(21) Zhang, H.; Zhai, T.; Yu, M.; Xie, S.; Liang, C.; Zhao, W.; Wang, S. C. I.; Zhang, Z.; Lu, X. TiO$_2$@C Core-Shell Nanowires for High-Performance and Flexible Solid-State Supercapacitors. *J.Mater.Chem. C* **2013**, *1*, 225−229.

(22) Ma, S. B.; Nam, K. W.; Yoon, W. S.; Yang, X. Q.; Ahn, K. Y.; Oh, K. H.; Kim, K. B. Electrochemical Properties of Manganese Oxide Coated onto Carbon Nanotubes for Energy-Storage Applications. *J. Power Sources* **2008**, *178*, 483−489.

(23) Komaba, S.; Ogata, A.; Tsuchikawa, T. Enhanced Supercapacitive Behaviors of Birnessite. *Electrochem. Commun.* **2008**, *10*, 1435−1437.

(24) Yan, J.; Fan, Z.; Wei, T.; Qian, W.; Zhang, M.; Wei, F. Fast and Reversible Surface Redox Reaction of Graphene-MnO$_2$ Composites As Supercapacitor Electrodes. *Carbon* **2010**, *48*, 3825−3833.

(25) Li, Z.; Wang, J.; Liu, S.; Liu, X.; Yang, S. Synthesis of Hydrothermally Reduced Graphene/MnO$_2$ Composites and Their Electrochemical Properties As Supercapacitors. *J. Power Sources* **2011**, *196*, 8160−8165.

(26) Zhang, Y.; Shi, E. W.; Chen, Z. Z.; Li, X. B.; Xiao, B. Large-Scale Fabrication of Silicon Carbide Hollow Spheres. *J. Mater. Chem.* **2006**, *16*, 4141−4145.

(27) Liu, Z.; Ci, L.; Jin-Phillipp, N. Y.; Ruhle, M. Vapor-Solid Reaction for Silicon Carbide Hollow Spherical Nanocrystals. *J. Phys. Chem. C* **2007**, *111*, 12517−12521.

(28) Socha, R. P.; Laajalehto, K.; Nowak, P. Influence of the Surface Properties of Silicon Carbide on the Process of SiC Particles Codeposition with Nickel. *Colloids Surf., A* **2002**, *208*, 267−275.

(29) Fan, Z.; Yan, J.; Wei, T.; Zhi, L.; Ning, G.; Li, T.; Wei, F. Asymmetric Supercapacitors Based on Graphene/MnO$_2$ and Activated Carbon Nanofiber Electrodes with High Power and Energy Density. *Adv. Funct. Mater.* **2011**, *21*, 2366−2375.

(30) Xu, C.; Wang, X.; Zhu, J. Graphene−metal Particle Nano-composites. *J. Phys. Chem. C* **2008**, *112*, 19841−19845.

(31) Zhang, X.; Sun, X.; Zhang, H.; Zhang, D.; Ma, Y. Development of Redox Deposition of Birnessite-Type MnO$_2$ on Activated Carbon As High-Performance Electrode for Hybrid Supercapacitors. *Mater. Chem. Phys.* **2012**, *137*, 290−296.

(32) Kim, M. J.; Hwang, Y. S.; Min, K. C.; Kim, J. H. Introduction of MnO$_2$ Nanoneedles to Activated Carbon to Fabricate High-Performance Electrodes As Electrochemical Supercapacitors. *Electrochim. Acta* **2013**, *113*, 322−331.

(33) Toupin, M.; Brousse, T.; Belanger, D. Charge Storage Mechanism of MnO$_2$ Electrode Used in Aqueous Electrochemical Capacitor. *Chem. Mater.* **2004**, *16*, 3184−3190.

(34) Gu, Y.; Cai, J.; He, M.; Kang, L.; Lei, Z.; Liu, Z. H. Preparation and Capacitance Behavior of Manganese Oxide Hollow Structures with Different Morphologies via Template-Engaged Redox Etching. *J. Power Sources* **2013**, *239*, 347−355.

(35) Chigane, M.; Ishikawa, M. Manganese Oxide Thin Film Preparation by Potentiostatic Electrolyses and Electrochromism. *J. Electrochem. Soc.* **2000**, *147*, 2246−2251.

(36) Toupin, M.; Brousse, T.; Belanger, D. Influence of Micro-structure on the Charge Storage Properties of Chemically Synthesized Manganese Dioxide. *Chem. Mater.* **2002**, *14*, 3946−3952.

(37) Song, M. K.; Cheng, S.; Chen, H.; Qin, W.; Nam, K. W.; Xu, S.; Yang, X. Q.; Bongiorno, A.; Bai, J.; Tyson, T. A.; Cho, J.; Liu, M. Anomalous Pseudocapacitive Behavior of a Nanostructured, Mixed-Valent Manganese Oxide Film for Electrical Energy Storage. *Nano Lett.* **2012**, *12*, 3483−3490.

(38) Mao, L.; Zhang, K.; Chan, H.; Wu, J. Nanostructured MnO$_2$/Graphene Composites for Supercapacitor Electrodes: The Effect of Morphology, Crystallinity and Composition. *J. Mater. Chem.* **2012**, *22*, 1845−1851.

(39) Kim, M. J.; Hwang, Y. S.; Kim, J. H. Super-Capacitive Performance Depending on Different Crystal Structures of MnO$_2$ in Graphene/MnO$_2$ Composites for Supercapacitors. *J. Mater. Sci.* **2013**, *48*, 7652−7663.

(40) Wu, Z. S.; Ren, W.; Wang, D. W.; Li, F.; Liu, B.; Cheng, H. M. High-Energy MnO$_2$ Nanowire/Graphene and Graphene Asymmetric Electrochemical Capacitors. *ACS Nano* **2010**, *4*, 5835−5842.

(41) Kim, M. J.; Hwang, Y. S.; Kim, J. H. Graphene/MnO$_2$-based Composites Reduced via Different Chemical Agents for Super-capacitors. *J. Power Sources* **2013**, *239*, 225−233.

(42) Casady, J. B.; Johnson, R. W. Status of Silicon Carbide (SiC) as a Wide-Bandgap Semiconductor for High-Temperature Applications: A Review. *Solid-State Electron.* **1996**, *39*, 1409−1422.

(43) Chen, S.; Zhu, J.; Wu, X.; Han, Q.; Wang, X. Graphene Oxide−MnO$_2$ Nanocomposites for Supercapacitors. *ACS Nano* **2010**, *4*, 2822−2830.

(44) Yoon, S. B.; Kim, K. B. Effect of Poly(3,4-ethylenedioxythio-phene) (PEDOT) on the Pseudocapacitive Properties of Manganese Oxide (MnO$_2$) in the PEDOT/MnO$_2$/Multiwall Carbon Nanotube (MWNT) Composite. *Electrochim. Acta* **2013**, *106*, 135−142.

(45) Xie, X.; Gao, L. Characterization of a Manganese Dioxide/Carbon Nanotube Composite Fabricated Using an in Situ Coating Method. *Carbon* **2007**, *45*, 2365−2373.

(46) Zhang, Y. J.; Sun, C. T.; Lu, P.; Li, K. Y.; Song, S. Y.; Xue, D. F. Crystallization Design of MnO$_2$ Towards Better Supercapacitance. *CrystEngComm* **2012**, *14*, 5892−5897.

(47) Zhu, G.; Deng, L. J.; Wang, J. F.; Kang, L. P.; Liu, Z. H. The simple Preparation of Birnessite-Type Manganese Oxide with Flower-Like Microsphere Morphology and Its Remarkable Capacity Retention. *Mater. Res. Bull.* **2012**, *47*, 3533−3537.

(48) Bordjiba, T.; Belanger, D. Direct Redox Deposition of Manganese Oxide on Multiscaled Carbon Nanotube/Microfiber Carbon Electrode for Electrochemical Capacitor. *J. Electrochem. Soc.* **2009**, *156*, A378−A384.

(49) Stoller, M. D.; Park, S.; Zhu, Y.; An, J.; Ruoff, R. S. Graphene-based Ultracapacitors. *Nano Lett.* **2008**, *8*, 3498−3502.

(50) Xiong, G.; Hembram, K. P. S. S.; Reifenberger, R. G.; Fisher, T. S. MnO$_2$-Coated Graphitic Petals for Supercapacitor Electrodes. *J. Power Sources* **2013**, *227*, 254−259.